

Final Technical Report

for

Investigation of Pressurized Wave Bearings

**NASA Grant Number
NAG3-2408**

Grant Duration
April 18, 2000 to December 31, 2003

Dr. Theo G. Keith, Jr.
Principal Investigator

Florin Dimofte
Co-Principal Investigator

Department of Mechanical, Industrial and Manufacturing Engineering
University of Toledo
Toledo, Ohio 43606

December 2003

Final Report for NASA grant NAG3-2408

Investigation of Pressurized Wave Bearings

by

Theo G. Keith, Jr. (Distinguished University Professor)
Florin Dimofte (Senior Research Associate)

Department of Mechanical, Industrial and Manufacturing Engineering
The University of Toledo, Toledo, Ohio 43606

PURPOSE

This grant supported research on gas (air) wave bearings for turbomachinery applications. A team of researchers from the University of Toledo performed the research. The team consists of Dr. Theo Keith (Distinguished University Professor), Dr. Florin Dimofte (Senior Research Associate) and Sorin Cioc (PhD Research Assistant).

INTRODUCTION

The wave bearing has been pioneered and developed by Dr. Dimofte over the past several years. This bearing will be the main focus of this research. It is believed that the wave bearing offers a number of advantages over the foil bearing, which is the bearing that NASA is currently pursuing for turbomachinery applications.

The wave bearing is basically a journal bearing whose film thickness varies around the circumference approximately sinusoidally, with usually 3 or 4 waves. Being a rigid geometry bearing, it provides precise control of shaft centerlines. The wave profile also provides good load capacity and makes the bearing very stable. Manufacturing techniques have been devised that should allow the production of wave bearings almost as cheaply as conventional full-circular bearings.

RESEARCH ACCOMPLISHMENTS

The research performed on this grant is described in the following 4 papers:

1. "Measured Gas Wave Journal Bearing Load Capacity at Steady Loads," (co-authors: F. Dimofte, and D.P. Fleming), presented at the 9th International Symposium on Transport Phenomena and Dynamics of Rotating Machinery (ISROMAC-9), Honolulu, Hawaii, February 10-14, 2002

2. "Computation of Pressurized Gas Bearings Using CE/SE Method," (co-authors: S. Cioc, F. Dimofte, and D. P. Fleming) *STLE Tribology Transactions* Vol. 46, No. 1, January 2003, pp 128-133.

3. "Application of the CE/SE Method to Wave Journal Bearings," (co-authors: S. Cioc, and F. Dimofte) *STLE Tribology Transactions* Vol. 46, No. 2, April 2003, pp. 179-186.

4. "Calculation of the Flow in High Speed Gas Bearings Including Inertial Effects Using the CE/SE Method," (co-authors: S. Cioc, F. Dimofte, and D. P. Fleming) presented at the 58th STLE Annual Meeting in New York, New York, April 28 – May 1, 2003

A copy of each of the first three papers is included below. Because the last paper is under review for publication in the *STLE Tribology Transactions* it is not included in this report.

MEASURED GAS WAVE JOURNAL BEARING LOAD CAPACITY UNDER STEADY LOADS.

Florin Dimofte, The University of Toledo, currently working at NASA Glenn Research Center, Cleveland, Ohio,

David P. Fleming, NASA Glenn Research Center, Cleveland, Ohio,

Theo G. Keith, Jr., The University of Toledo.

ABSTRACT

A 35 mm diameter by 28 mm long wave air bearing was tested at speeds up to 30,000 rpm. The tests were performed on a gas bearing rig at NASA Glenn Research Center in Cleveland, Ohio. A maximum load of 196 N was supported by the bearing at maximum speed for more than 90 minutes. The bearing was stable both dynamically and thermally. Good agreement was found with numerical prediction.

INTRODUCTION

A circular (plain) journal bearing has better load capacity than all other hydrodynamic journal bearings if the comparison criteria is the minimum film thickness. However, the plain journal bearing is easily de-stabilized, especially if the bearing is unloaded. This has been proven both theoretically and experimentally [1, 2, 3]. To improve stability, the plain journal bearing's geometry must be modified.

Numerous concepts including lobed, grooved, stepped, and tilting-pad bearings were developed. These concepts, however, have substantially lower load capacity. The wave bearing, a new concept developed at NASA Glenn Research Center, offers good stability with a load capacity that is close to that of a plain journal bearing [4]. The wave journal bearing features a wave profile circumscribed on the inner bearing diameter. The wave bearing can have 2, 3 or more waves, and the wave amplitude can vary. However a three wave bearing was found to better satisfy both steady-state and dynamic running conditions than other wave bearing geometries [5, 6]. A three-wave bearing concept is shown in fig. 1a. A plain journal bearing is shown in fig. 1b for comparison. The wave amplitude and bearing clearance are exaggerated so that the wave profile can be seen.

Predictive analysis was developed to quantify the performance of wave journal bearings and contrast it to plain

journal bearings [4]. The predictions revealed a significant difference in the pressure distribution between the three-wave and the plain journal bearing. The altered pressure distribution provides a higher load capacity for the wave bearing when compared to the plain circular bearing operating at the same eccentricity [4]. In addition, the wave journal bearing offers better stability. The analysis was performed assuming that the bearings were operating in air, a compressible lubricant. This analysis was validated by the measurements performed on a bench test rig that was assembled at NASA Glenn Research Center [7]. The work presented herein was performed to establish the practical maximum load capacity of a wave bearing that could also be compared to other types of air bearings.

DESCRIPTION OF TEST RIG

An air bearing test rig (fig. 2) was built to test journal bearings with 30-50 mm diameters and 25-60 mm lengths. A commercial air spindle (fig. 2, pos. 4) with a removable add-on shaft is used to drive the test bearing. It is mounted vertically to eliminate gravitational effects. The spindle can operate at rotational speeds to 30,000 rpm with a shaft run-out of less than 40 micro-inches (1 micron). A cross section of the bearing assembly is presented in fig. 3. The mechanical run-out of the add-on shaft (fig. 3, pos 4) was measured with a contact electronic dial indicator, accurate to 0.1 μm . The run-out of the add-on shaft is less than 0.2 μm at the top (farthest from the spindle) and less than 0.1 μm at the bottom (closest to the spindle).

The test bearing set up can be seen in fig. 4. The test bearing housing (fig. 3, pos. 1 or fig. 4, pos. 1) is supported between two air thrust plates (fig 4, pos.2 and 3). The thrust plates allow the test bearing to move freely in the radial direction. The bottom thrust plate (fig. 4, pos. 2) was designed with 3 thrust pads to allow bearing alignment to the shaft. Each pad has a separate air supply system including a valve (regulator) and pressure gauge. The top thrust plate (fig. 4, pos.3) contains a single 360 degree pad. It is supported by three threaded rods (fig. 4, pos. 4) which allow easy adjustment to the axial clearance of both (bottom and top) thrust

plates.

The bearing rotor (fig. 3, pos. 5) is mounted on the top of the add-on shaft. The bearing sleeve is assembled inside the bearing sleeve assembly (fig. 3, pos. 2). The bearing sleeve assembly is fixed inside the housing (fig. 3, pos. 1). Rubber O-rings are used between the bearing sleeve assembly and the housing to provide additional self-alignment capability when load is applied. The test bearing was operated in ambient air.

A radial load can be applied to the test bearing via a pneumatic load cylinder (fig. 2, pos. 2). A micro-switch (fig. 4, pos. 5) is used to sense excessive torque on the bearing housing; it will shut off the spindle if triggered. A burst shield surrounds the experimental bearing for added safety.

The test rig includes instrumentation to measure shaft speed, radial load, rotor-sleeve position, and bearing temperature. Shaft speed is measured by a capacitive probe located within the spindle. A miniature precision load cell (fig. 2, pos. 3 or fig. 4, pos. 6) measures the radial load applied by the pneumatic load cylinder. Two light beam displacement sensors (fig. 4, pos. 7) allow measurement of rotor-sleeve position. The bearing housing temperature is monitored with K-type thermocouples (fig. 4, pos. 8).

TEST RESULTS

The tested bearing has a 35 mm diameter and is 28 mm long. The radial clearance was 18 μm and the ratio of the wave amplitude to radial clearance is 0.143. Since the goal of this work was to establish a maximum practical load capacity of the wave journal bearing, the bearing was tested under relatively large loads. Consequently, large eccentricity to radial clearance ratios (greater than 0.7) resulted. Speeds of 5000, 10,000, 20,000, and 30,000 rpm were used. Eccentricity, shaft speed, and load were recorded at each load step by using a digital camera. A typical photograph containing this information can be seen in fig. 5. This figure also shows the maximum load applied to the bearing in this test, 44 lb (196 N), at a maximum shaft speed of 29,418 rpm where the bearing operated with 15.8 μm eccentricity. The bearing temperature was also monitored. At maximum speed the bearing temperature stabilized at 33°C in a few minutes and was then virtually constant throughout the tests, which ranged up to 90 minutes.

The results of this test are plotted in fig. 6 in terms of specific load (average bearing pressure) versus eccentricity ratio. Analytical predictions are also plotted. Figure 6 shows that the wave bearing ran at eccentricity ratios from 0.7 to 0.88. The bearing ran stably at all speeds, and bearing temperature stabilized in a short time at reasonable values for each run. The wave bearing can carry a specific load of 2 bars at 30,000 rpm.

CONCLUDING REMARKS

A 35 mm diameter by 28 mm long wave air bearing was tested at speeds up to 30,000 rpm in the hydrodynamic regime. The test was performed on the gas bearing rig at NASA Glenn Research Center in Cleveland, Ohio.

A maximum load of 196 N was carried by the bearing at maximum speed (30,000 rpm) for more than 90 minutes. This corresponds to a specific load of 2 bars. The bearing was stable both dynamically and thermally.

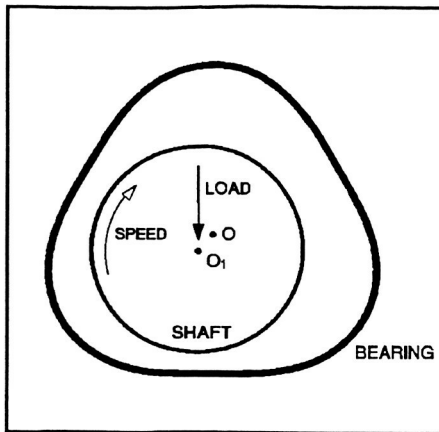
Good agreement was found with numerical prediction.

ACKNOWLEDGMENT

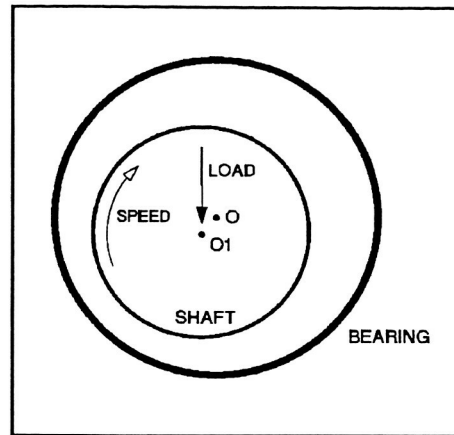
This work was performed at NASA Glenn Research Center in Cleveland, Ohio as part of a Director's Discretionary Fund project.

REFERENCES

1. Constantinescu, V. N., *Gas Lubrication*, ASME, New York, 1969.
2. Szeri, A. Z., *Fluid Film Lubrication*, Hemisphere Publishing Corporation, Washington D.C., 1980.
3. Gross, W.A., *Fluid Film Lubrication*, John Wiley & Sons, New York, 1980.
4. Dimofte, F., "Wave Journal Bearing with Compressible Lubricant; Part I: The Wave Bearing Concept and a Comparison to the Plain Circular Bearing", *STLE Tribology Trans.* Vol. 38, No. 1, 1995, pp.153-160.
5. Dimofte, F., "A Waved Journal Bearing Concept with Improved Steady-State and Dynamic Performance", presented at The 7th Workshop on Rotordynamic Instability, May 10-12, 1993, Texas A&M University, College Station, TX., published in *Rotordynamic Instability Problems in High-Performance Turbomachinery*, NASA CP 1036, 1993, pp. 419-429.
6. Dimofte, F., and Hendricks, R.C., "Three-Wave Gas Bearing Behavior with Shaft Runout", *Proceedings of the Eighth Workshop on Rotordynamic In-stability Problems in High-Performance Turbomachinery* held at Texas A&M University, College Station, TX, May 6 - 8, 1996, pp. 5 - 13.
7. Dimofte, F., Addy, H.E., Jr., and Walker, J.F., "Preliminary Experimental Results of a Three Wave Journal Air Bearing", *Proceeding of Advanced Earth-to-Orbit Propulsion Technology Conference* held at NASA Marshall Space Flight Center, Huntsville, AL, May 17-19, 1994, NASA CP 3282, Vol 11, 1994, pp.375-384.



a. Three Wave



b. Circular

Figure 1. Journal Bearings.

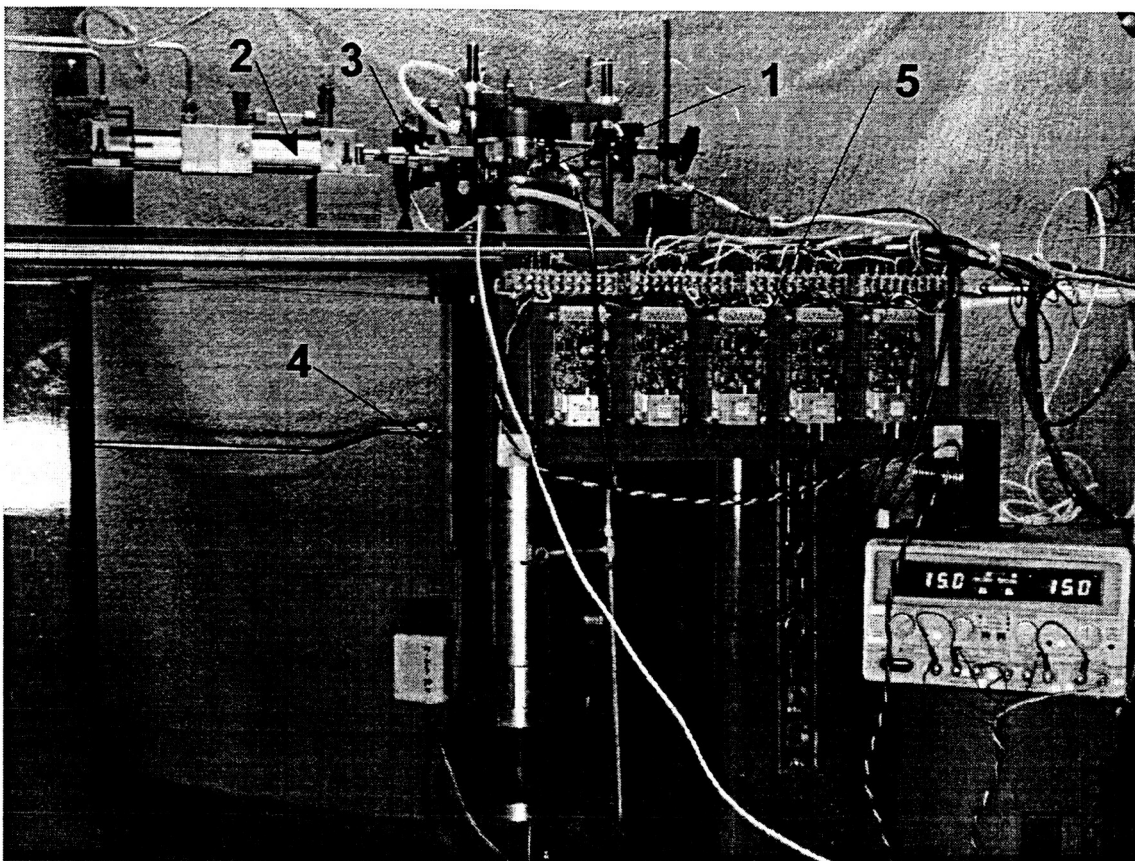


Figure 2. Gas Wave Bearing Rig: 1 Test Bearing; 2 Pneumatic Load Cylinder; 3 Load Cell; 4 Air Spindle; 5 Light Beam Displacement Sensor Signal Conditioners.

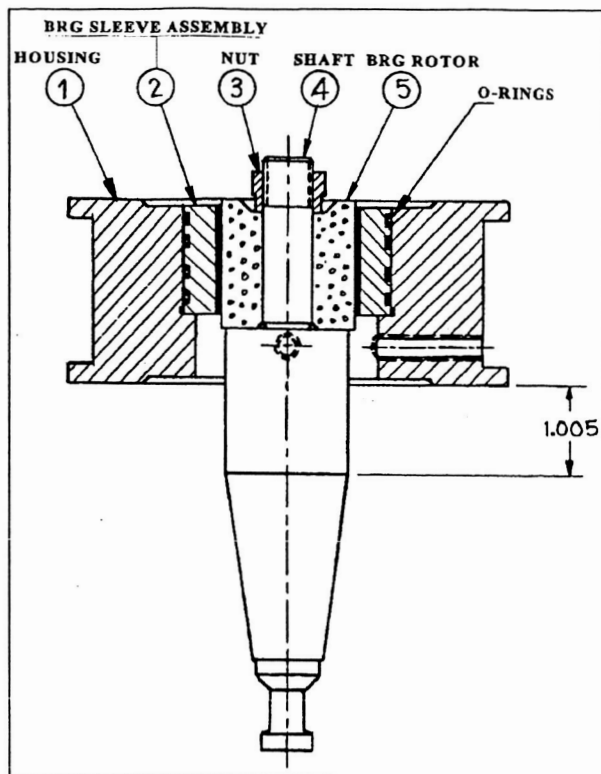


Figure 3. Bearing Assembly Cross Section

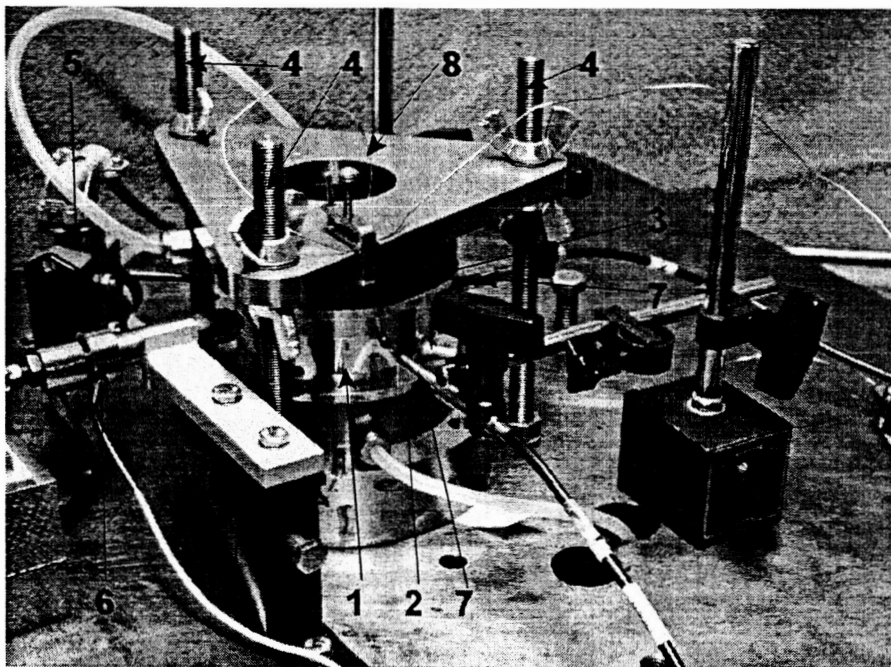


Figure 4. Test Bearing: 1 Housing; 2 Bottom Thrust Plate; 3 Top Thrust Plate; 4 Threaded Rods; 5 Micro-switch; 6 Load Cell; 7 Displacement Sensors; 8 Thermocouple Line.

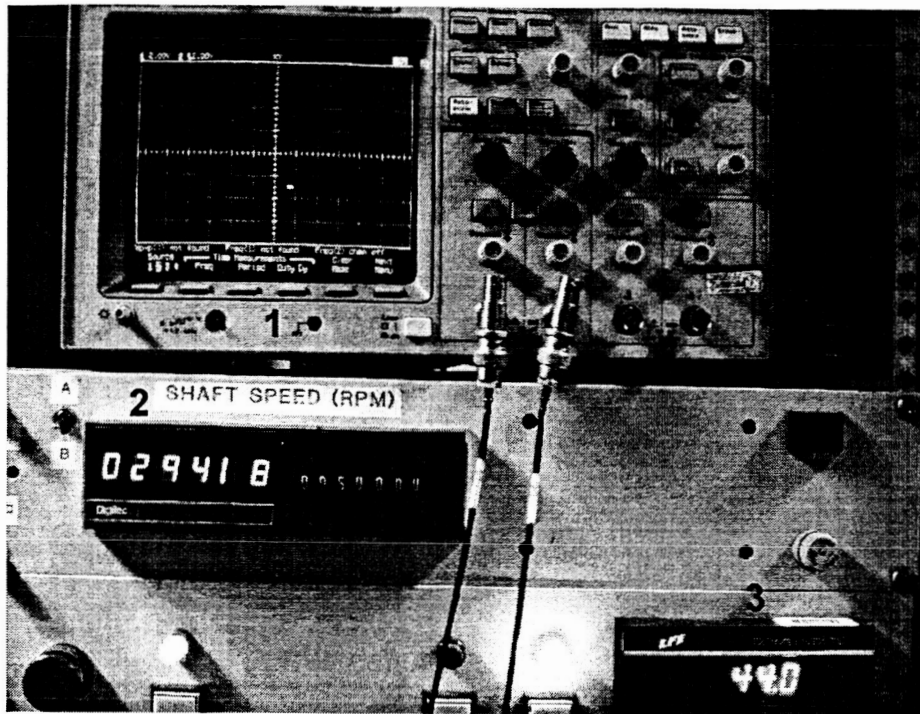


Figure 5. Records at Max Speed and Max Load: 1 Eccentricity ($10\mu\text{m}/\text{div}$); 2 Shaft Speed (rpm); 3 Load (lb)

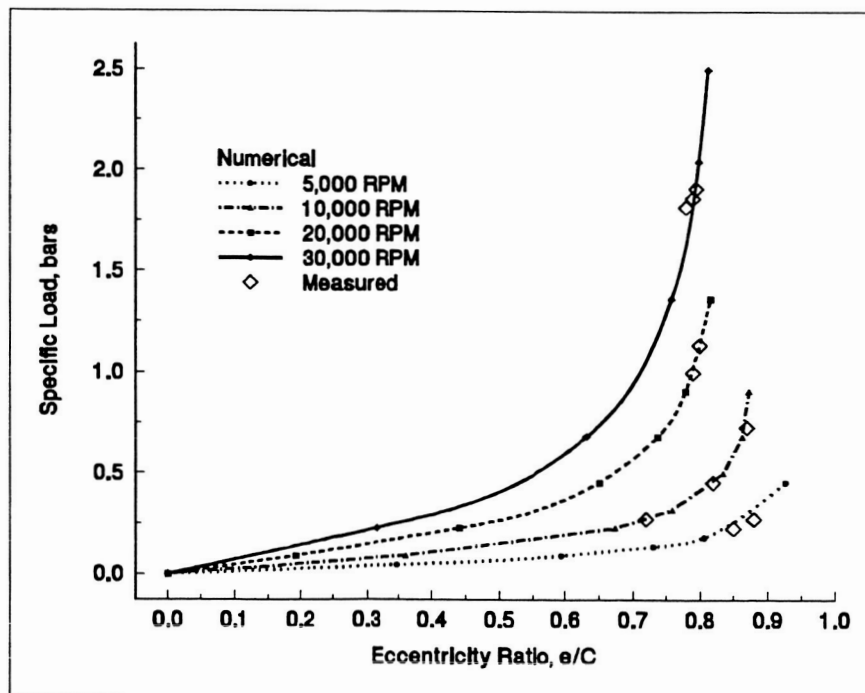


Figure 6. Specific Loads vs. Eccentricity Ratios: Comparison of Measurement to Prediction.



Computation of Pressurized Gas Bearings Using the CE/SE Method[©]

SORIN CIOC, FLORIN DIMOFTE and THEO G. KEITH, JR.

The University of Toledo

Department of Mechanical Engineering

Toledo, Ohio

and

DAVID P. FLEMING

NASA Glenn Research Center

Cleveland, Ohio

A numerical scheme that has been successfully used to solve a wide variety of compressible flow problems, including flows with large and small discontinuities, entitled the space-time conservation element and solution element (CE/SE) method, is extended to

compute compressible viscous flows in pressurized thin fluid films. This method is applied to calculate the pressure distribution in a hybrid gas journal bearing. The formulation of the problem is presented, including the modeling of the feeding system. The numerical results obtained are compared with experimental data. Good agreement between the computed results and the test data were obtained, and thus, validate the CE/SE method to solve such problems.

Presented at the 57th Annual Meeting
in Houston, Texas

May 19-23, 2002

Final manuscript approved September 5, 2002

Review led by R. Gordon Kirk

NOMENCLATURE

a	= radius of the feeding orifice
a_F, b_F, c_F	= coefficients in the Taylor series expression of function f
a_G, b_G, c_G	= coefficients in the Taylor series expression of function g
C	= radial clearance
D	= diameter of the feeding pocket
e	= eccentricity
\vec{F}	= $f\vec{i} + g\vec{k}$ Vector flux term
f	= circumferential flux term, see Eq. [5]
g	= axial flux term, see Eq. [5]
h	= film thickness (dimensional)
\bar{h}	= h/C non-dimensional film thickness
\vec{i}, \vec{k}	= unit vectors in circumferential and in axial directions, respectively
L	= length of the bearing
n	= Adiabatic coefficient
n_w	= number of waves (for wave bearings)
ns	= number of feeding holes
p	= fluid pressure
\bar{p}	= p/p_0 non-dimensional pressure
p_0	= atmospheric (reference) pressure
p_s	= supply pressure
Q	= mass flow rate through one feeding hole
\bar{Q}	= non-dimensional mass flow rate through one feeding hole – see Eq. [17]
R	= journal bearing radius
t	= time
\bar{t}	= $t \frac{p_0}{\mu} (\frac{C}{R})^2$ non-dimensional time

u	= $\bar{h}\bar{p}$ dependent variable in the governing equation
U	= ωR velocity in circumferential direction
\bar{U}	= $\frac{\mu\omega}{2\pi p_0} (\frac{R}{C})^2$ non-dimensional circumferential velocity
x	= circumferential coordinate
\bar{x}	= $x/(2\pi R)$ non-dimensional circumferential coordinate
\bar{x}_0	= position of the maximum fluid film thickness, measured in the negative direction of axis \bar{x}
\bar{x}_w	= position of the wave peak (for wave bearings), measured in the negative direction of axis \bar{x}
z	= axial coordinate
\bar{z}	= $z/(2\pi R)$ non-dimensional axial coordinate
γ	= Isentropic exponent
Δt	= time step
ε	= weight parameter characterizing one form of artificial dissipation, or e/C eccentricity ratio
ε_w	= wave amplitude (for wave bearings)
μ	= fluid viscosity
ρ	= fluid density
$\bar{\rho}$	= ρ/ρ_0 non-dimensional fluid density
ρ_0	= atmospheric (reference) density
ω	= angular velocity of the journal bearing

SUBSCRIPTS AND SUPERSSCRIPTS, OTHER THAN SHOWN ABOVE

$()_0$	= value of the variable at the point O
$()_i$	= supply pocket index
$()_{,x}, ()_{,z}, ()_{,t}$	= partial derivative with respect to x , z , and t , respectively
$()^n$	= time step

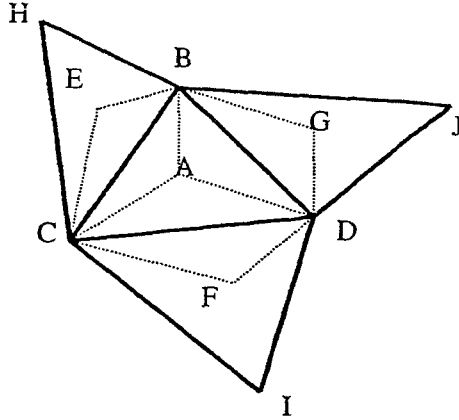


Fig. 1—Triangular mesh element and its neighbors.

KEY WORDS

Bearings; Gas; Hydrostatic Lubrication; Flow Rate

INTRODUCTION

Gas lubrication, though preceded by occasional experimental work since the mid 19th century, experienced a strong development in the "Golden Era" of gas lubrication, which started in the last years of World War II, and ended in the first part of the 70's (12). In this period much important work was published: (9)–(11), (2), (6). More recently, significant advancements were reported in gas film modeling including rarefaction effects, (13), in numerical methods applicable to high-speed bearings, (8), and particularly in the treatment of complex geometries, including discontinuities, (1).

The space-time conservation element and solution element (CE/SE) method was proposed by (3). Over the past several years it has been utilized in a number of fluid flow applications that involve shock waves, contact discontinuities, acoustic waves, vortices and chemical reactions. One of its main features is that it can simultaneously capture small and large discontinuities (such as sound waves and shock waves) without introducing numerical oscillations into the solution, as shown by (5), (4).

Compressible viscous flow in pressurized thin fluid films, with application in hybrid gas bearings, can encounter large pressure gradients due to the feeding system or to the large peripheral velocities of the bearing. In these conditions, the computational methods based on standard finite difference methods or classic finite volume methods may prove inadequate having convergence problems or inducing oscillations into the solution. Thus, a method that is conceptually simple, is second order accurate for the entire domain and is able to naturally deal with large gradients and/or discontinuities in the solutions without introducing numerical oscillations or smearing, is welcome.

ANALYSIS

The two-dimensional, transient, Reynolds equation, written for a Newtonian compressible fluid in laminar flow is,

$$\frac{\partial \rho h}{\partial t} + \frac{\partial}{\partial x} \left(\frac{\rho h U}{2} - \frac{\rho h^3}{12\mu} \frac{\partial p}{\partial x} \right) + \frac{\partial}{\partial z} \left(-\frac{\rho h^3}{12\mu} \frac{\partial p}{\partial z} \right) = 0 \quad [1]$$

The flow is considered polytropic, i.e.,

$$\frac{p}{\rho^n} = \text{const.}, \quad [2]$$

where the polytropic exponent is $n = 1$ for isothermal flow, $n = 1.405$ for adiabatic flow, or can have other values for general polytropic flows.

A more suitable form of the Reynolds equation for numerical formulation is obtained using a new variable u that is the product of the non-dimensional film thickness and the pressure, i.e.,

$$u = \bar{h}\bar{p} \quad [3]$$

In terms of u , in non-dimensional variables, the Reynolds equation can be written as

$$\frac{\partial u}{\partial t} + \frac{\partial f}{\partial \bar{x}} + \frac{\partial g}{\partial \bar{z}} = 0 \quad [4]$$

where the flux terms f and g are,

$$f = \frac{u\bar{U}}{2} - \frac{nu^n}{48\pi^2\bar{h}^{n-1}}(u_x\bar{h} - u\bar{h}_x),$$

$$g = -\frac{nu^n}{48\pi^2\bar{h}^{n-1}}(u_z\bar{h} - u\bar{h}_z). \quad [5]$$

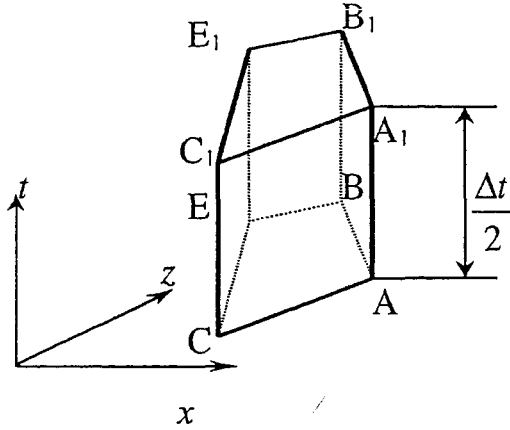
All partial derivatives considered in Eqs. [4] and [5] are carried out relative to non-dimensional variables $\bar{t}, \bar{x}, \bar{z}$. In the following, in order to simplify the expressions, the non-dimensional notation (upper bar) will be dropped, and all variables will be implicitly considered in non-dimensional form.

Consider a triangular mesh that covers the (x, z) spatial domain. One triangle BCD and its three neighboring elements are shown in Fig. 1. Point A is the centroid of the triangle BCD , while points E, F and G are the centroids of the neighboring triangles BCH, CDI and BDJ , respectively. The CE/SE method calculates the values of the dependent variables u, u_x, u_z for point A at the time step $t = t^{n+\frac{1}{2}}$ using the corresponding values of the same variables for the points E, F and G at the time step $t = t^n$. In order to calculate the three unknowns at the new time step, a system of three equations will be derived.

Consider the quadrilateral $ABEC$. Simultaneously integrating Eq. [4] over the surface of this quadrilateral and in time, between time steps t^n and $t^{n+\frac{1}{2}}$ (see Fig. 2), yields

$$\int \int_{ABEC} \int_{t^n}^{t^{n+\frac{1}{2}}} \frac{\partial u}{\partial t} dt d\sigma + \int_{t^n}^{t^{n+\frac{1}{2}}} \int \int_{ABEC} \left[\frac{\partial f}{\partial \bar{x}} + \frac{\partial g}{\partial \bar{z}} \right] d\sigma dt = 0. \quad [6]$$

Performing the time integration for the first term and transforming the surface integration into a contour integration for the second term (using Green's theorem) produces

Fig. 2—Conservation volume in the (x, z, t) space.

$$\int \int_{ABEC} (u^{n+\frac{1}{2}} - u^n) d\sigma + \int_{t^n}^{t^{n+\frac{1}{2}}} \oint_{ABEC} \vec{F} \cdot \vec{n} ds dt = 0, \quad [7]$$

where \vec{n} is the unit vector normal to the contour, oriented outwards and

$$\vec{F} = f\vec{i} + g\vec{k} \quad [8]$$

is the vector in the (x, z) plane characterized by the Cartesian unit vectors (\vec{i}, \vec{k}) . Functions f and g are given by Eq. [5]. Equation [7] implies conservation of flux in the three-dimensional space (x, z, t) . Functions u, f, g are next written with linear approximations using first order Taylor expansions, i.e.,

$$u \cong u_0 + (u_x)_0(x - x_0) + (u_z)_0(z - z_0) + (u_t)_0(t - t_0), \quad [9]$$

$$f \cong f_0 + \left(\frac{\partial f}{\partial u}\right)_0(u - u_0) + \left(\frac{\partial f}{\partial u_x}\right)_0[u_x - (u_x)_0] + \left(\frac{\partial f}{\partial u_z}\right)_0[u_z - (u_z)_0] = a_F u + b_F u_x + c_F, \quad [10]$$

$$g \cong g_0 + \left(\frac{\partial g}{\partial u}\right)_0(u - u_0) + \left(\frac{\partial g}{\partial u_x}\right)_0[u_x - (u_x)_0] + \left(\frac{\partial g}{\partial u_z}\right)_0[u_z - (u_z)_0] = a_G u + b_G u_x + c_G. \quad [11]$$

Substituting Eq. [9] into Eqs. [10] and [11] yields linear expressions for f and g as functions of (x, z, t) . In Eqs. [10] and [11], coefficients $a_F, b_F, c_F, a_G, b_G, c_G$ are considered constant when integrating Eq. [7], and are known as functions of $u_0, (u_x)_0, (u_z)_0$. In Eq. [9], the time derivative can be calculated as function of the space derivatives using Eq. [3], i.e.,

$$(u_t)_0 = -(f_x)_0 - (g_z)_0 \cong -a_F(u_x)_0 - a_G(u_z)_0. \quad [12]$$

Equations [8]-[12] are then substituted into Eq. [7]. Point $(x_{A'}, z_{A'}, t^{n+\frac{1}{2}})$ is used as the Taylor expansion point for the expressions of $u^{n+\frac{1}{2}}, f$ and g on the contour segments AB and CA ,

while point $(x_{E'}, z_{E'}, t^n)$ is used as the Taylor expansion point for the expressions of u^n, f and g on the contour segments BE and EC . Thus, a first equation with three unknowns, the values u, u_x, u_z at the new half time step $(x_{A'}, z_{A'}, t^{n+\frac{1}{2}})$, is obtained. The coordinates of points A' and E' are selected in a suitable way, as will be shown later. The equation is linear and has the general form

$$a_1 u_{A'}^{n+\frac{1}{2}} + b_1 (u_x)_{A'}^{n+\frac{1}{2}} + c_1 (u_z)_{A'}^{n+\frac{1}{2}} + d_1 u_{E'}^n + e_1 (u_x)_{E'}^n + f_1 (u_z)_{E'}^n + g_1 = 0. \quad [13a]$$

Two other similar equations are obtained using the same procedure for the conservation elements $ACFD$ and $ADGB$. These equations have the general form

$$a_2 u_{A'}^{n+\frac{1}{2}} + b_2 (u_x)_{A'}^{n+\frac{1}{2}} + c_2 (u_z)_{A'}^{n+\frac{1}{2}} + d_2 u_{F'}^n + e_2 (u_x)_{F'}^n + f_2 (u_z)_{F'}^n + g_2 = 0. \quad [13b]$$

$$a_3 u_{A'}^{n+\frac{1}{2}} + b_3 (u_x)_{A'}^{n+\frac{1}{2}} + c_3 (u_z)_{A'}^{n+\frac{1}{2}} + d_3 u_{G'}^n + e_3 (u_x)_{G'}^n + f_3 (u_z)_{G'}^n + g_3 = 0. \quad [13c]$$

The linearized system formed by Eqs. [13a], [13b], and [13c] can be solved using an iterative method; note that the coefficients $a_i, b_i, c_i, i = 1, 2, 3$ are functions of the unknowns $u_{A'}^{n+\frac{1}{2}}, (u_x)_{A'}^{n+\frac{1}{2}}, (u_z)_{A'}^{n+\frac{1}{2}}$. An alternate approach is to choose the Taylor series expansion point A' as the center of the hexagon $BECFDG$. The other three Taylor series expansion points E', F', G' can be chosen arbitrarily; however, in order to maintain consistency, they are selected as the centers of the corresponding hexagons formed around the neighboring triangular elements.

Adding Eqs. [13a], [13b], and [13c] yields a new equation that represents the flux conservation over the hexagon and over one half time step. When point A' is the centroid of the hexagon $BECFDG$, this equation has a simpler form given by

$$a_{sum} u_{A'}^{n+\frac{1}{2}} + d_1 u_{E'}^n + e_1 (u_x)_{E'}^n + f_1 (u_z)_{E'}^n + d_2 u_{F'}^n + e_2 (u_x)_{F'}^n + f_2 (u_z)_{F'}^n + d_3 u_{G'}^n + e_3 (u_x)_{G'}^n + f_3 (u_z)_{G'}^n + g_{sum} = 0, \quad [14]$$

where a_{sum} is given by

$$a_{sum} = A_{ABEC} + A_{ACFD} + A_{ADGB} = A_{BECFDG} \quad [15]$$

Equation [14] has only one unknown, $u_{A'}^{n+\frac{1}{2}}$, and can easily be solved explicitly. It is also important to note that all the coefficients in Eq. [14] depend only on the geometry (coordinates of the points) and the values of the dependent variables at the previous half time step so that an iterative method is not needed. After calculating the value $u_{A'}^{n+\frac{1}{2}}$, the values of the other two dependent variables $(u_x)_{A'}^{n+\frac{1}{2}}$ and $(u_z)_{A'}^{n+\frac{1}{2}}$ can be calculated using any two of the Eqs. [13a], [13b], and [13c]. This is also called the a scheme.

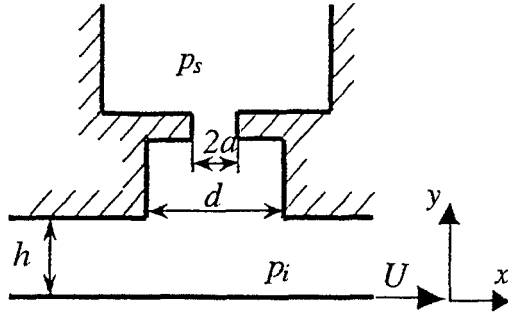


Fig. 3—Feeding orifice geometry.

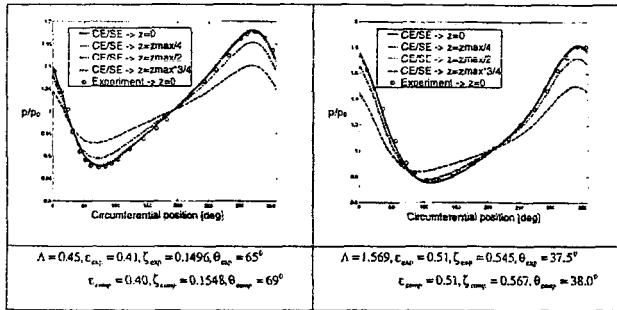


Fig. 4—Comparison between numerical and experimental results for the pressure distribution in a gas journal bearing (2 pictures).

Note that the a scheme introduces “no significant damping” ((5), (4)), so that some form of artificial dissipation is generally necessary. The scheme can be simplified and simultaneously stabilized by calculating the space derivatives in a different way. The scheme thus obtained is called the $a - \epsilon - \alpha - \beta$ scheme. In this scheme, the derivatives are calculated as weighted averages between the derivatives calculated from the governing equations, as shown above (the a scheme), the derivatives calculated using 2-D central difference finite difference formulae (weight parameter ϵ) and the derivatives using 2-D side finite differencing (weight parameter β). Parameter α is the power index used in the computation of the non-linear weighted average that employs 2-D side finite differencing. The complete formulation of the way the derivatives are calculated in the $a - \epsilon - \alpha - \beta$ scheme can be found in (4). It is important that, for a certain value of the weighting parameter ϵ ($\epsilon = 0.5$), the $a - \epsilon - \alpha - \beta$ scheme eliminates the necessity of calculating the space derivatives from the governing equations, thus the method becomes purely explicit.

The feed system, formed by a number of ns orifices with the general geometry shown in Fig. 3, can be modeled using a generally accepted formula, (10), (11), that links the mass flow ratio to the feed system geometry and the pressures at the ends of the feed system considering both effects of the orifice restrictor and the inherent restrictor, i.e.,

$$Q = \frac{\pi a^2 \sqrt{p_s \rho_s}}{\sqrt{1 + (\frac{a}{2h})^2}} \bar{Q} \quad [16]$$

where the non-dimensional mass flow \bar{Q} is a fraction C_D of the ideal mass flow,

$$\bar{Q} = C_D \begin{cases} \sqrt{\gamma (\frac{2}{\gamma+1})^{\frac{\gamma+1}{\gamma-1}}} & \text{for } \frac{p_i}{p_s} \leq (\frac{2}{\gamma+1})^{\frac{\gamma}{\gamma-1}} \\ \sqrt{\frac{2\gamma}{\gamma-1} (\frac{p_i}{p_s})^{\frac{2}{\gamma}} [1 - (\frac{p_i}{p_s})^{\frac{\gamma-1}{\gamma}}]} & \text{for } (\frac{2}{\gamma+1})^{\frac{\gamma}{\gamma-1}} < \frac{p_i}{p_s} \leq 1 \end{cases} \quad [17]$$

When no restricting orifice is present, i.e., an inherent restrictor, Eq. [16] becomes

$$Q = \pi d h \sqrt{p_s \rho_s} \bar{Q} \quad [18]$$

The feeding system is introduced into the bearing computation through the boundary conditions. Thus, on each feeding pocket contour, the mass flow rates calculated from the bearing equations and from the feeding system, respectively, must be equal

$$(Q_i)_{\text{bearing}} = (Q_i)_{\text{feeding}}, \quad i = 1, 2, \dots, ns. \quad [19]$$

Equation [19] represents a nonlinear set of ns equations, where the pressures in the bearing at the feeding holes are the unknowns p_i , $i = 1, 2, \dots, ns$. This system is solved iteratively using Newton's method.

RESULTS AND DISCUSSION

A computer code has been developed based on the described method, using the $a - \epsilon - \alpha - \beta$ scheme with $\epsilon = 0.5$. This code has been tested for some simple cases where experimental data were available, considering isothermal flow ($n = 1$).

The first case considered was the circular gas bearing without any feeding system. The results are shown in Fig. 4, where the same bearing with the aspect ratio $L/(2R) = 2.0$ is examined for two bearing numbers $\Lambda = (6\mu\omega R^2)/(p_0 C^2)$ and for two eccentricities. There are no significant differences between the experimental and calculated pressure distributions, at least in the middle plane where the experimental results are available. The relative differences between the experimental and calculated non-dimensional loads $\zeta = \text{Load}/(p_0 2LR)$ are 3.5% and 4.0%; both represent improvements over the theoretical results shown by (6).

The second case considered is the wave journal bearing (7) without any feed system. The fluid film thickness in an aligned wave bearing is given as,

$$\bar{h} = 1 + \epsilon \cos 2\pi(\bar{x} + \bar{x}_0) + \epsilon_w \cos[2\pi n_w(\bar{x} + \bar{x}_w)] \quad [20]$$

In the last term on the right hand side of Eq. [19], ϵ_w is the wave amplitude, n_w is the number of waves and \bar{x}_w is the wave origin relative to the origin of the \bar{x} axis. For the present case, the bearing diameter and bearing length are 50 mm, the radial clearance is 0.02 mm, $n_w = 3$, $\epsilon_w = 0.3$, and the relative minimum film thickness is $\bar{h}_{\min} = 0.3$ for all cases. The bearing number is 3.566.

The results are compared with a finite difference based code built by (7). Different bearing positions (\bar{x}_w) have been tested and the results (calculated load magnitude and position) are presented

TABLE 1—COMPARISON BETWEEN CALCULATED DATA WITH CE/SE METHOD AND WITH FINITE DIFFERENCE METHOD

ECCENTRICITY	α_w (deg)	LOAD CE/SE (N)	LOAD FD (N)	LOAD ANGLE CE/SE (deg)	LOAD ANGLE FD (deg)
0.502	40	177	177	40.49	40.18
0.460	32	170	170	39.09	38.8
0.433	24	166	165	36.37	36.11
0.416	16	163	162	32.94	32.69
0.404	8	158	158	29.30	29.06
0.400	0	154	154	25.61	25.38
0.404	-8	151	151	22.08	21.86
0.416	-16	149	148	18.95	18.75

TABLE 2—PRESSURIZED GAS BEARING GEOMETRY AND WORKING CONDITIONS

Bearing length (mm)	117.5
Bearing diameter (mm)	60.4
Supply planes	2
Supply plane position (mm)	12.7
Holes/supply plane	14
Orifice diameter (mm)	0.16
Pocket diameter (mm)	0.9
Supply pressure (Pa)	5.514×10^5
Injection angle (deg)	90

in Table 1. The results show very good agreement between the two methods.

The third case considered is a pressurized gas bearing without rotation and with zero eccentricity. Details of the bearing geometry and working conditions are presented in Table 2. Figures 5(a) and 5(b) show the calculated and experimental pressure distributions for two values of the radial clearance, corresponding to the subsonic flow regime (obtained when $C = 12.7 \mu\text{m}$), and the choked flow regime (obtained when $C = 31.75 \mu\text{m}$) in the feed system, in two longitudinal planes situated at the jet position (Fig. 5(a)) and at half distance between jets (Fig. 5(b)); pressure peaks are visible at the jet positions; also nearly constant pressure is obtained between the supply planes. The predicted pressure peaks at the position of the jet are higher than the experimental values (this difference is more visible for the subsonic inlet flow, however it is present in both cases). This is due to the difficulty of measuring the local pressure at the feeding orifice position. The value for the correction factor C_D is 0.8 for the subsonic inlet flow, and 0.85 for the choked flow.

Finally, the code was applied to different configurations, where experimental or computed data were not available.

Figure 6 shows the pressure distribution (sections at the jet and at the mid-jet positions) obtained for five supply planes for the same bearing as in the previous case $C = 12.7 \mu\text{m}$. The supply planes are equally distanced with respect to each other and with the bearing ends. It is seen that, although the external pressure is the same for all supply holes, the pressure that develops in the pockets (inside the bearing) is not the same for all supply planes.

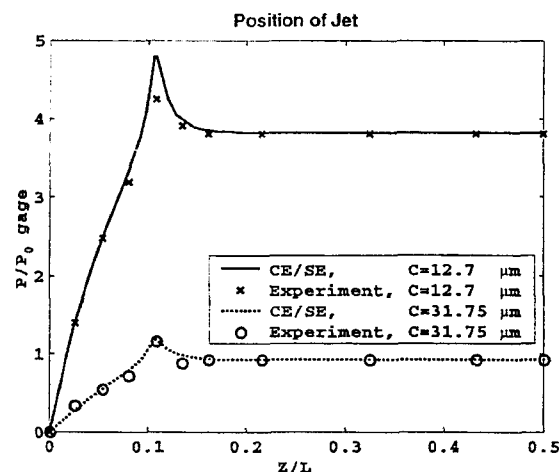


Fig. 5(a)—Comparison between the calculated and experimental pressure distributions at jet position.

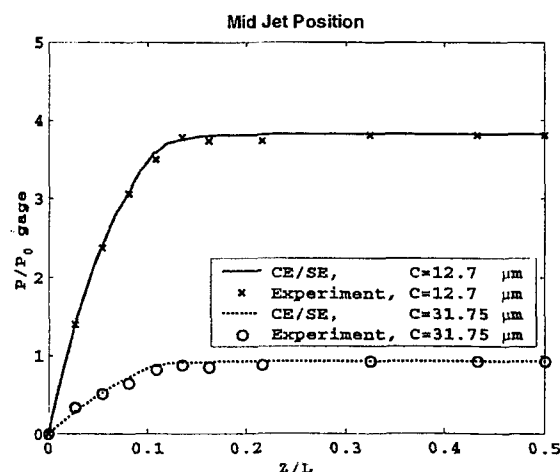


Fig. 5(b)—Comparison between the calculated and experimental pressure distributions at mid-jet position.

The pressure distribution between two consecutive feeding planes has an almost linear form. Furthermore, at the central supply

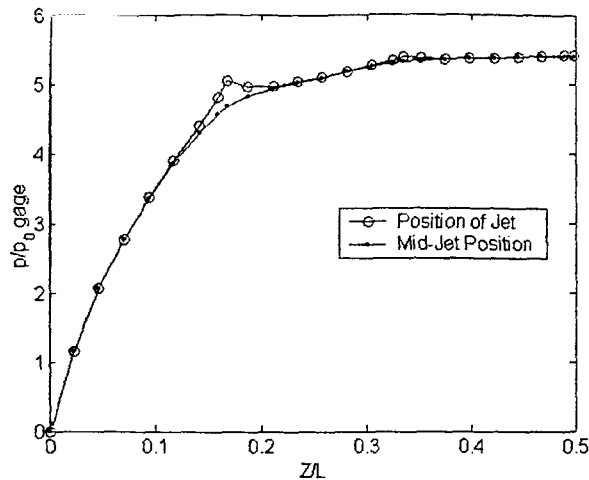


Fig. 6—Pressure distribution for a circular bearing without eccentricity, with five supply planes.

plane, the peak pressures are not as visible as the peak pressures at the other supply planes; this suggests that the central supply plane does not have an important contribution for the general pressure distribution inside the bearing.

Figure 7 shows the pressure distribution in half bearing for the same bearing geometry as in the previous two cases, but in a running condition (40,000 RPM, $\Lambda = 25.76$), with a relative eccentricity $\epsilon = 0.5$. The value $C_D = 0.8$ was used. The pressure distribution is very complex. It can be seen that for many feeding holes the flow is inverted, i.e., is directed from the bearing towards the feeding system, because the pressure inside the bearing is higher than the supply pressure.

CONCLUSIONS

The CE/SE computational method has been extended for the first time to calculate compressible viscous flow in pressurized thin fluid films with restrictors in series. Formulation of the method was presented along with the numerical results obtained for both non-pressurized and pressurized bearings. The results were compared with existing experimental and computed data. The results demonstrate the ability of the method to accurately predict the pressure distributions in such flows.

While most numerical methods handle space and time differencing terms in the governing equations separately, this relatively new scheme treats them in a unified way. This results in very good accuracy even though the unknowns are considered locally linear and even when a relatively coarse grid is used. Also, the entire structure of the method, as well as the developed code, are relatively simple. Unlike most numerical schemes, no special treatment is necessary for discontinuities, providing that the governing equations are written in strong conservative form. However, the method is limited to time dependent equations. Steady state results, such as those discussed in this work, can be obtained only after the stabilization of the unsteady solution starting from initial conditions.

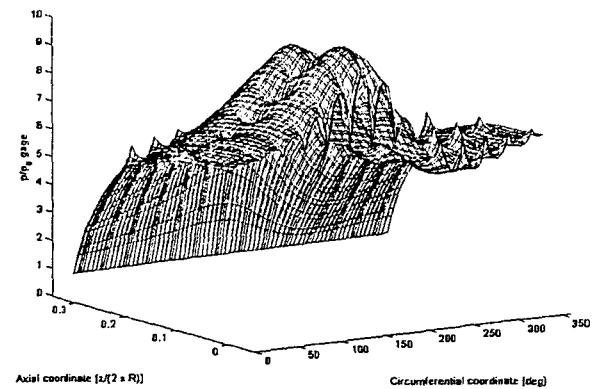


Fig. 7—Pressure distribution for a circular bearing with eccentricity, with five supply planes.

Future work will focus on predicting dynamic characteristics of pressurized gas bearings. Improving the feeding system with restrictors in series modeling will also be considered, as well as improving the computation time. Cases including discontinuities will also be considered.

REFERENCES

- (1) Bonneau, D., Huitric, J. and Tournerie, B. (1993), "Finite Element Analysis of Grooved Gas Thrust Bearings and Grooved Gas Face Seals," *Jour. of Trib., Trans. ASME*, **115**, 3, pp 348-354.
- (2) Castelli, V. and Pirvics, J. (1968), "Review of Numerical Methods in Gas Bearing Film Analysis," *Jour. of Lubr. Tech., Trans. ASME*, **90**, pp 777-792.
- (3) Chang, S. C. and To, W. M. (1991), "A New Numerical Framework for Solving Conservation Laws - The Method of Space-Time Conservation Element and Solution Element," NASA TM 104495, NASA, Cleveland, OH.
- (4) Chang, S. C., et al. (1998), "Fundamentals of CE/SE Method," NASA TM-1998-208843, PDF file.
- (5) Chang, S. C., Wang, X. Y. and Chow, C. Y. (1999), "The Space-Time Conservation Element and Solution Element Method: A New High-Resolution and Genuinely Multidimensional Paradigm for Solving Conservation Laws," *Jour. of Comp. Phys.*, **156**, 1, pp 89-136.
- (6) Constantinescu, V. N. (1969), "Gas Lubrication," American Society of Mechanical Engineers, Wehe, R. L., ed., New York, pp 455-467.
- (7) Dimofte, F. (1995), "Wave Journal Bearing with Compressible Lubricant; Part I: The Wave Bearing Concept and a Comparison to the Plain Circular Bearing," *STLE Trib. Trans.*, **38**, 1, pp 153-160.
- (8) Faria, M. T. C. and San Andrés, L. (2000), "On the Numerical Modeling of High-Speed Hydrodynamic Gas Bearings," *Trans. ASME*, **122**, 1, pp 124-130.
- (9) Fuller, D. D. (1956, 1984), "Theory and Practice of Lubrication for Engineers," New York, Wiley.
- (10) Lund, J. W. (1964), "The Hydrostatic Gas Journal Bearing With Journal Rotation and Vibration," *Jour. of Basic Engineering, Trans. ASME*, **86**, June, pp 328-336.
- (11) Lund, J. W. (1967), "A Theoretical Analysis of Whirl Instability and Pneumatic Hammer for a Rigid Rotor in Pressurized Gas Journal Bearings," *Jour. of Lubr. Tech., Trans. ASME*, **89**, April, pp 328-336.
- (12) Pan, Coda H. T. (1990), "Gas Lubrication (1915-1990)," *Achievements in Tribology: on the 75th Anniversary of the ASME Research Committee on Tribology*, Trib. Vol. 1, pp 31-55.
- (13) Wu, L. and Bogoy, D.B. (2001), "Numerical Simulation of the Slider Air Bearing Problem of Hard Disk Drives by Two Multidimensional Upwind Residual Distribution over Unstructured Triangular Meshes," *Jour. of Computational Physics*, **172**, 2, pp 640-657.



Application of the CE/SE Method to Wave Journal Bearings[©]

SORIN CIOC, FLORIN DIMOFTE and THEO G. KEITH, JR.

The University of Toledo

Mechanical, Industrial and Manufacturing Engineering Department

Toledo, Ohio 43606

The space-time conservation element and solution element (CE/SE) method, successfully used to solve a wide variety of compressible flow problems, is extended for the first time to predict the effects of gaseous cavitation in moderate to heavily loaded wave bearings, including misaligned cases. Elrod's formulation is used for a two-dimensional, finite length bearing, and the intricacies of the CE/SE scheme applied to solve this problem are presented. The numerical results obtained are compared with other numerical solutions to demonstrate the ability of the method to solve such problems.

Presented as a Society of Tribologists and Lubrication Engineers Paper at the ASME/STLE Tribology Conference in Cancun, Mexico

October 27-30, 2002

Final manuscript approved January 29, 2003

Review led by Luis San Andres

KEYWORDS

Bearings; Hydrodynamic; Cavitation

INTRODUCTION

The space-time conservation element and solution element (CE/SE) method was proposed for the first time by Chang and To (1). Over the past several years it has been utilized in a number of fluid flow applications that involve shock waves, contact discontinuities, acoustic waves, vortices and chemical reactions. Being capable of simultaneously capturing small and large discontinuities (such as sound waves and shock waves) without introducing numerical oscillations in the solution (2)-(4) this new method is an excellent candidate to be applied to the flow in cavitated wave bearings.

Historically, the most common practice to account for the effects of cavitation in fluid film bearings was through the application of the Gumbel (or half-Sommerfeld) boundary conditions. This was accomplished by setting negative pressures to zero (rel-

NOMENCLATURE

a	= coefficient in the flux term f (see Eq. [4]), m/s
b	= coefficient in the flux terms f and g (see Eq. [4]), m ² /s
c	= coefficient in the flux term g (see Eq. [4]), m/s
C	= radial clearance, m
d_m	= degree of misalignment, non-dimensional
f	= Flux term in x direction (see Eq. [3]), m ² /s
\vec{F}	= $f\vec{i} + g\vec{k}$ vector flux term
g	= flux term in z direction (see Eq. [3]), m ² /s
g_c	= switch function (see Eq. [5]), non-dimensional
h	= film thickness, m
\vec{i}, \vec{k}	= unit vectors in circumferential and in axial directions, respectively.
L	= bearing length, m
\vec{n}	= unit vector normal on the contour line, oriented outwards
p	= fluid pressure, Pa
R	= bearing radius, m
s	= linear (contour) coordinate, m

t	= time, s
u	= $h\theta$, m
U	= velocity in circumferential direction (ωR), m/s
x	= circumferential coordinate, m
z	= axial coordinate, m
α	= angle between the centerline and the direction of the misalignment at the bearing center
β	= bulk modulus, Pa
Δt	= time step, s
μ	= fluid viscosity, Pa·s
θ	= ρ/ρ_c , non-dimensional density in full film; fractional film content in cavitated region
ω	= angular velocity of the journal bearing, s ⁻¹

SUBSCRIPTS AND SUPERSSCRIPTS

$()_0$	= value of the variable in the point O
$()_c$	= value at the cavitation border
$()_{x'}, ()_{z'},$	
$()_t$	= partial derivative with respect to x , z , and t , respectively.

ative to the cavitation pressure). Although the load carrying predictions by this approach were reasonably accurate, the results violated the mass conservation principle. Consequently, several other procedures have been proposed. Jakobsson and Floberg (5) and later Olsson (6) introduced a self-consistent, mass conservative, set of boundary conditions for cavitation to be applied to Reynolds equation. This procedure is valid for moderately to heavily loaded bearings and is generally called JFO theory. This methodology is commonly incorporated into modern computational algorithms for bearings, and is also implicitly included in the present method.

Previous computational methods used for this problem are known to have certain difficulties. Elrod's algorithm (7) was the first that correctly applied JFO theory, however the algorithm necessitated, as the author pointed out, "considerable experimentation" to develop. Moreover, it has only first order accuracy in the cavitated region, while in the full film region the algorithm is accurate to second order; an oscillation in the cavitation front is often found to occur. The method proposed in (8) is based on concepts used in transonic flow (9). This method uses a number of features from the Elrod algorithm, but does not "rely on experimentation" to develop the solver. It should be noted that the Vijayaraghavan and Keith method has the same accuracy as the Elrod's algorithm in cavitated regions and in the full film region. In addition, like Elrod's method, the solver loses accuracy at the cavitation boundaries.

In this context, a method such as the CE/SE scheme, which is conceptually simple and has the capacity to accurately predict the fluid film flow including the boundaries of the cavitated region(s), without numerical oscillations or smearing, represents an improvement over these earlier methods. This is especially important since, as shown in (10) for the one-dimensional case, the theoretical formulation can lead to flow discontinuities at the reformation front. The CE/SE method applied to the Reynolds equation has some noticeable advantages: it is second order accurate over the entire domain, it computes in a unified way the pressure induced flow for all the regions and, because it solves a set of integral equations derived directly from the physical conservation laws, the scheme is able to capture naturally the flow discontinuities (cavitation boundaries). Thus, the CE/SE method can potentially provide better results for the cavitation and reformation front positions, as well as for the distributions of the state variables in their vicinity. This paper presents the general development of the CE/SE method applied to two-dimensional cavitated flows in journal bearings, showing the strengths and some of the limitations of this emerging modern computational scheme. The paper also presents some results obtained using this numerical scheme to illustrate its characteristics.

ANALYSIS

The theoretical model, based on Reynolds equation in Elrod's formulation, is the two-dimensional extension of the formulation presented in (10). In strong conservation form, required for a weak solution (with discontinuities), the governing equation is,

$$\frac{\partial u}{\partial t} + \frac{\partial f}{\partial x} + \frac{\partial g}{\partial z} = 0 \quad [1]$$

The main unknown u is the product of the film thickness, h , and the non-dimensional density, θ ,

$$u = h\theta \quad [2]$$

Note that the non-dimensional density θ has also the meaning of fractional film content in the cavitated region. The flux terms are given by the following expressions,

$$\begin{aligned} f &= au - b \frac{\partial u}{\partial x} \\ g &= cu - b \frac{\partial u}{\partial z} \end{aligned} \quad [3]$$

where coefficients a , b , and c are

$$\begin{aligned} a &= \frac{U}{2} + g_c \frac{\beta h}{12\mu} \frac{\partial h}{\partial x} \\ b &= g_c \frac{\beta h^2}{12\mu} \\ c &= g_c \frac{\beta h}{12\mu} \frac{\partial h}{\partial z} \end{aligned} \quad [4]$$

The value of the switch function g_c is determined by the value of θ ,

$$g_c = \begin{cases} 1 - \text{full film region, } \theta \geq 1 \\ 0 - \text{cavitated region } \theta < 1 \end{cases} \quad [5]$$

The governing equation is spatially elliptic in the full film region and hyperbolic in the cavitated region.

In order to numerically solve the problem using the CE/SE method, the main unknown u and the flux terms f and g are written in linear form using a Taylor series. Considering a generic point of expansion O , they are written as

$$u \cong u_0 + (u_x)_0(x - x_0) + (u_z)_0(z - z_0) + (u_t)_0(t - t_0) \quad [6]$$

$$f \cong f_0 + (f_x)_0(x - x_0) + (f_z)_0(z - z_0) + (f_t)_0(t - t_0)$$

$$g \cong g_0 + (g_x)_0(x - x_0) + (g_z)_0(z - z_0) + (g_t)_0(t - t_0) \quad [7]$$

Because the time derivative u_t can be written from the governing equation in terms of space derivatives, Eq. [6] can also be expressed as

$$u \cong u_0 + (u_x)_0(x - x_0) + (u_z)_0(z - z_0) - (f_x + g_z)_0(t - t_0) \quad [8]$$

Solution of the governing equation, Eq. [1], is performed on a triangular mesh in the (x, z) plane. One triangle BCD and its three neighbor elements are shown in Fig. 1. Point A is the centroid of the triangle BCD , while points E , F and G are the centroids of the neighboring triangles BCH , CDI and BDJ . The CE/SE method calculates the values of the variable u , for a "representative point" A of the triangle BCD , at the new time step $t = t^{n+1}$ using the corresponding values of the same variables for the points E , F and G at the old time step $t = t^n$. The location of the "representative

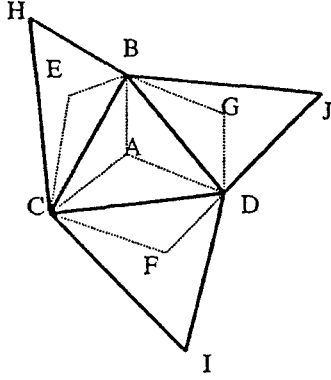


Fig. 1—Triangular mesh element and its neighbors.

points" A' , E' , F' , and G' will be explained later. In order to calculate the unknown at the new time step, one equation will be derived. This equation can be obtained considering the hexagon $BECFDG$. Simultaneously integrating the governing equation, Eq. [1], over the surface of this hexagon and in time, between time steps t^n and t^{n+1} , yields

$$\int_{BE} \int_{CFD} \int_{t^n}^{t^{n+1}} \frac{\partial u}{\partial t} dt dx dz + \int_{t^n}^{t^{n+1}} \int_{BE} \int_{CFD} \left(\frac{\partial f}{\partial x} + \frac{\partial g}{\partial z} \right) dx dz dt = 0 \quad [9]$$

Equation [9] implies flux conservation in the three-dimensional space (x, z, t) , which represents the central feature of the method, also justifying its name. Performing the time integration for the first term and transforming the surface integration into a contour integration for the second term (using Green's theorem) yields,

$$\int_{BE} \int_{CFD} (u^{n+1} - u^n) dx dz + \int_{t^n}^{t^{n+1}} \oint_{BECFD} \vec{F} \cdot \vec{n} ds dt = 0 \quad [10]$$

where \vec{n} is the outward directed unit vector, normal to the contour, and

$$\vec{F} = f\vec{i} + g\vec{k} \quad [11]$$

is a vector in the (x, z) plane characterized by the Cartesian unit vectors (\vec{i}, \vec{k}) .

Because functions u , f , and g are substituted with linear approximations, given by Eqs. [7] and [8], the time integral in Eq. [10] can be written as the value of the integrand at the mid-interval multiplied with the length of the time step, i.e.,

$$\int_{BE} \int_{CFD} (u^{n+1} - u^n) d\sigma + \Delta t (\oint_{BECFD} \vec{F} \cdot \vec{n} ds)^{n+1/2} = 0 \quad [12]$$

The next important feature of the method consists in selecting the "representative point" for each triangular element as the centroid of the hexagon constructed around that triangular element. In this case, point A' is the centroid of hexagon $BECFDG$, while points E' , F' , and G' are the centroids of the hexagons corresponding to the neighbor elements.

The integrals that appear in Eq. [12] are calculated using the linear approximations, given by Eqs. [7], and [8]. The points of expansion are as follows:

- Point A' for the first term in Eq. [12], which is approximated as,

$$\int_{BE} \int_{CFD} u^{n+1} d\sigma \cong u_{A'}^{n+1} A_{BECFD} \quad [13]$$

- Point E' for all the integrals that include the quadrilateral $ABEC$, and similarly, point F' for the quadrilateral $ACFD$, and point G' for the quadrilateral $ADGB$. The surface integral $\int_{BE} \int_{CFD} u^n d\sigma$ is written as the sum of the surface integrals over the three mentioned quadrilaterals, each of them with its own expansion point, thus,

$$\int_{BE} \int_{CFD} u^n d\sigma = \int_{AB} \int_{EC} u^n d\sigma + \int_{AC} \int_{FD} u^n d\sigma + \int_{AD} \int_{GB} u^n d\sigma \quad [14]$$

For example, the first integral in the right hand side of Eq. [14] is written as,

$$\int_{AB} \int_{EC} u^n d\sigma \cong \int_{AB} \int_{EC} [u_{E'}^n + (u_x)_{E'}(x - x_{E'}) + (u_z)_{E'}(z - z_{E'})] dx dz \quad [15]$$

Since all the terms are evaluated at the old time step n , the right hand side can be determined numerically. Similarly, the contour integral $\oint_{BECFD} \vec{F} \cdot \vec{n} ds$ is written as the sum of six segment integrals,

$$\begin{aligned} \oint_{BECFD} \vec{F} \cdot \vec{n} ds &= \left(\int_{BE} \vec{F} \cdot \vec{n} ds + \int_{EC} \vec{F} \cdot \vec{n} ds \right)_{E'} + \\ &\left(\int_{CF} \vec{F} \cdot \vec{n} ds + \int_{FD} \vec{F} \cdot \vec{n} ds \right)_{F'} + \\ &\left(\int_{DG} \vec{F} \cdot \vec{n} ds + \int_{GB} \vec{F} \cdot \vec{n} ds \right)_{G'} \end{aligned} \quad [16]$$

The right hand side of Eq. [16] was written in segregated form to indicate that each group of terms uses one expansion point. For example, point E' is used as expansion point for the integrals over the segments BE and EC , etc. All the line integrals are calculated using the values at the old time step, which are readily available. For example,

$$\begin{aligned} \left(\int_{BE} \vec{F} \cdot \vec{n} d\sigma \right)^{n+1/2} &= \\ \int_{BE} &[\vec{F}_{E'}^n + (\vec{F}_x)_{E'}(x - x_{E'}) + \\ &(\vec{F}_z)_{E'} + (\vec{F}_z)_{E'}(z - z_{E'}) + (\vec{F}_t)_{E'} \frac{\Delta t}{2}] \cdot \vec{n} d\sigma \end{aligned} \quad [17]$$

At the end of this process, one explicit equation is obtained. It contains only one unknown, viz., the value of u^{n+1} at the new time step.

After calculating the field of the unknown u at the new time step, the space derivatives u_x and u_z must also be calculated. This

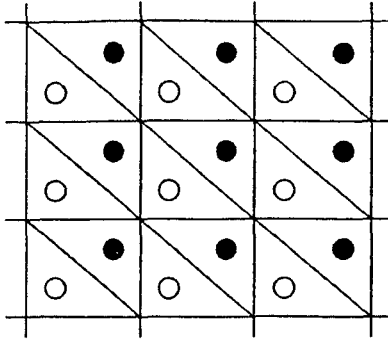


Fig. 2—Uniform triangular mesh.

task is accomplished by using an averaging combination of central and side differencing approximations. This procedure insures a minimum, but necessary, amount of numerical dissipation. For more information about the calculation of the space derivatives, the reader should consult (11) and (12).

An important feature is that, even though the space derivatives are not calculated from the conservation condition (the integrated form of Reynolds equation), this is still satisfied over the surface of each hexagonal element and in time (conservation volume).

The flux terms derivatives f_x, f_z, g_x, g_z can be calculated following an identical procedure. Another approach, which was also used, considers, starting from Eq. [3], and neglecting higher order terms, so that

$$\begin{aligned} (f_x)_0 &\cong (u_x)_0, (f_z)_0 \cong a_0(z)_0, (f_t)_0 \cong a_0(u_t)_0 = -a_0^2(u_x)_0 - a_0 c_0(u_z)_0 \\ (g_x)_0 &\cong c_0(u_x)_0, (g_z)_0 \cong c_0(u_z)_0, (g_t)_0 \cong c_0(u_t)_0 = -a_0 c_0(u_x)_0 - c_0^2(u_z)_0 \end{aligned} \quad [18]$$

These approximations have the advantage of simplifying the calculations, without significantly reducing the accuracy of the method.

An interesting feature of the method consists in the fact that the value of the unknown at the new time step for any element is calculated using exclusively the values at the old time step for the neighboring elements. Figure 2 shows a portion of simple uniform triangular mesh. Assuming that the values of u at the time step n are known for all elements marked with black dots, at the time $n+1$, the values of u for all elements marked with hollow circles can be calculated. At the next time step, $n+2$, the values for the black dot elements can be calculated. It is thus evident that the method actually uses two staggered grids, and at each time step it switches from one grid to the other. In practice, both grids can be used at every time step. This procedure doubles the volume of calculations, but it has the advantages of producing better resolution of the results, as well as permitting the extension of the applicability of the method for general unstructured grids. Another advantage is related to the calculation of the space derivatives, as shown in (12).

As with most explicit methods applied to hyperbolic partial differential equations, the stability of the method is subject to the

CFL condition (13), which states that the ratio between the time step and the space step must be small enough (more exact, the maximum Courant number, which is the product of this ratio and the local velocity, must be smaller than 1). Also, when the time step (Courant number) decreases, the accuracy of the method decreases, because the dissipation increases. For the present problem, the Courant number is multi-dimensional and variable in the field. In addition, the governing equation is second order, necessitating the calculation of an equivalent Courant number. Because of these features, a different approach is used. In this methodology, the time step is determined using a heuristic procedure, so that it simultaneously satisfies the following conditions: (i) when the time step is increased, by a factor of two for instance, the scheme becomes unstable, and (ii) when the time step is decreased, by a factor of two for example, the results do not change significantly (the change is due only to a small increase of the dissipation – smearing of the solution). This approach is directly derived from the general characteristics of explicit numerical methods, and it was found to be very effective. An example of a detailed approach for the convergence and error bound analysis of this method applied at a more simple equation can be found in (16). The use of a variable time step did not bring any significant benefit.

RESULTS AND DISCUSSION

In order to determine the performance of the method, numerical solutions in several geometries were performed. The results were compared with the results obtained using other numerical methods. Only the asymptotic steady state solution, obtained by time integration until the state parameters stabilize, was considered. The grids used consisted of 90-180 intervals in the circumferential direction (a coarser grid can be used for simple geometries), 10-20 intervals in the axial direction for a half bearing, 20-40 intervals for a full bearing (misaligned cases). The grids used are uniform in both directions, and the results show no significant change for the grid intervals specified. The non-dimensional time step $\bar{t} = \omega t$ has the order of 10^{-5} . 30,000-120,000 time steps were usually needed to obtain the steady solution (residual of variable u smaller than $10^{-4} - 10^{-5}$). The computational time required to obtain the steady-state solution starting from an initial uniform pressure distribution ranged from 5 to 25 minutes on a 1 GHz PC.

Circular Journal Bearing

A standard journal bearing with one inlet groove was first considered. The geometry and the fluid characteristics are presented in Table 1.

Figures 3 and 4 show a comparison between the non-dimensional gage pressure, $\bar{p} = \frac{p}{\mu\omega} \left(\frac{C}{R}\right)^2$, and the fractional fluid film content, θ , distributions obtained with the CE/SE method and with the type difference method (9), (14). Two transverse sections through the bearing at $z = 0$ and $z = L/4$ are presented for each method. The bearing z coordinate ranges between the values $-L/2$ and $L/2$, so that $z = 0$ is the symmetry plane. The differences between the two methods are seen to be relatively small; the maximum pressure predicted using type differencing is less than 2% lower than the maximum pressure calculated with the present method, while the total load is 6.9% lower. The difference

TABLE 1—PHYSICAL CONDITIONS FOR CIRCULAR JOURNAL BEARING

PARAMETER	VALUE	UNITS
Length	62.8×10^{-3}	m
Diameter	62.8×10^{-3}	m
Clearance	40.0×10^{-6}	m
Relative eccentricity	0.8	-
Groove position	0	deg
Supply pressure (gage)	1.355×10^6	Pa
Angular velocity, ω	628.32	s^{-1}
Viscosity	0.0035	Pa s
Bulk Modulus, β	5.421×10^7	Pa
Cavitation pressure (gage)	0	Pa

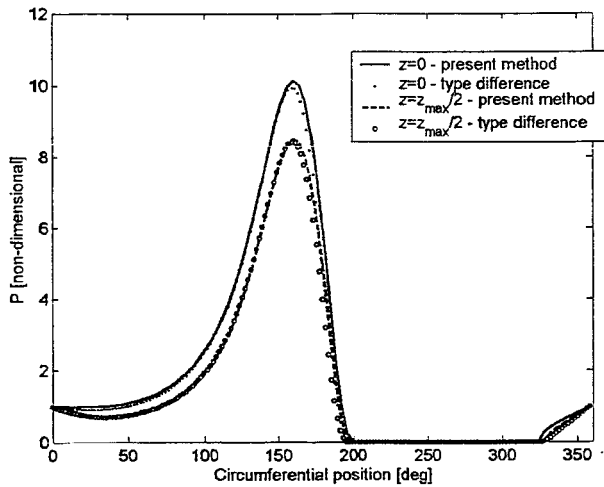


Fig. 3—Pressure distribution for a circular journal bearing with one inlet groove.

between the attitude angles calculated with the two methods is 0.9° .

Figure 4 shows that for the cavitated region, $\theta < 1$, the type differencing method produces a sharper discontinuity in the fractional film content compared to the CE/SE method. However, in the type differencing code, the discontinuity in the fractional film content distribution is forced to occur using different numerical formulations for the two different regions – full film, and cavitation, respectively. The computational domain is accordingly split into two parts, connected through boundary conditions. On the other hand, the computational domain used by CE/SE code is continuous (periodic boundary conditions are used at one circumferential position), so that the fractional film content discontinuity appears in the field. Also, no special treatment is used for any of the two regions. This approach was possible only because the CE/SE method is able to cope with large discontinuities without introducing any significant amount of numerical smearing and/or oscillations. The code developed using the CE/SE method is thus more general and potentially more robust. The visible presence of numerical dissipation is due to the small time step, which is necessary to obtain the CFL stability condition in the full film regions. This dissipation affects only the value of θ in the cavitated region in the vicinity of a discontinuity, which is unimportant

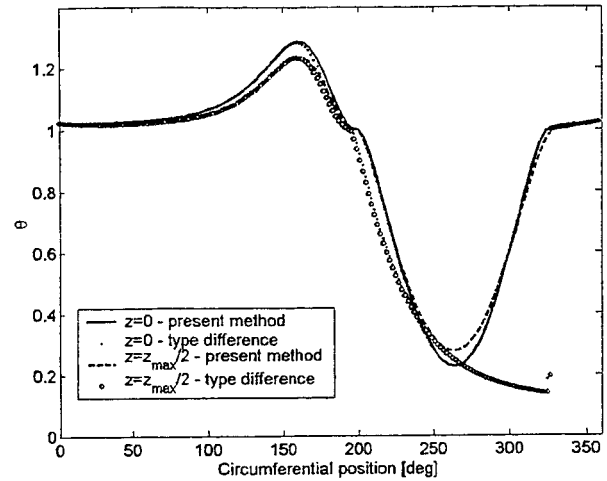


Fig. 4—Fractional film content distribution for a circular journal bearing with one inlet.

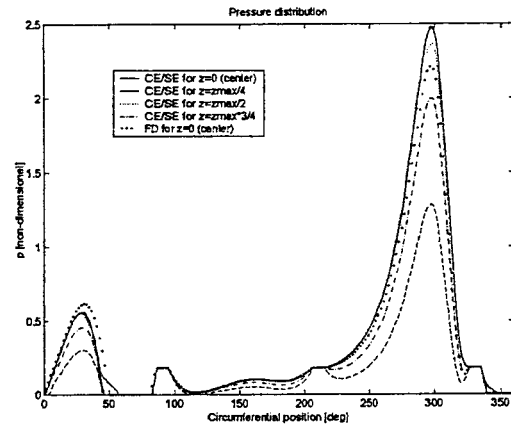


Fig. 5—Pressure distribution in a wave bearing.

relative to the pressure distribution, since $p = p_c = \text{const.}$ in these regions.

Wave Journal Bearing

The geometry of a wave bearing is more complex compared with the geometry of a standard journal bearing, Dimofte (15). An example of the non-dimensional film thickness $\bar{h} = h/C$ distribution for a three-wave bearing as a function of the circumferential coordinate is shown in Fig. 7(b), as discussed later. The physical conditions are presented in Table 2.

Figure 5 shows the non-dimensional gage pressure $\bar{p} = \frac{p}{\mu\omega} \left(\frac{C}{R}\right)^2$ distribution obtained using the present method compared with the pressure calculated by Dimofte, using a finite difference (FD) method to solve the steady form of Reynolds equation with Gümbel (or half-Sommerfeld) boundary conditions. The results show similar variations, however the peak pressures differ. The total load predicted by the present method is 2039 N, 13.7% higher than the load predicted using FD, which indicates a lower numerical dissipation for the CE/SE method. The difference

PARAMETER	VALUE	UNITS
Length	26.0×10^{-3}	m
Diameter	45.0×10^{-3}	m
Clearance	15.0×10^{-6}	m
Number of supply pockets	3	-
Pocket positions	86, 206, 326	deg
Pockets width	4.0	mm
Supply pressure (gage)	5.458×10^5	Pa
Angular velocity, ω	413.85	s^{-1}
Viscosity	0.00325	Pa s
Density	902.0	Kg/m^3
Bulk Modulus, β	1.2105×10^8 1.0290×10^7	Pa

PARAMETER	VALUE	UNITS
Length	45.0×10^{-3}	m
Diameter	45.0×10^{-3}	m
Clearance	15.0×10^{-6}	m
Angle of misalignment	90	deg
Degree of misalignment	0.5, 0	-
Number of supply pockets	1	-
Pocket position	80	deg
Pocket width	4.0×10^{-3}	m
Supply pressure (gage)	5.458×10^5	Pa
Angular velocity, ω	413.85	s^{-1}
Viscosity	0.00325	Pa s
Bulk Modulus, β	1.2105×10^8	Pa

between the predicted load directions using the two codes is less than 1.6° . These results have been obtained using a bulk modulus value $\beta = 1.2105 \cdot 10^8$ Pa. The pressure distribution using a smaller value, $\beta = 1.029 \cdot 10^7$ Pa, is presented in Fig. 6. In this case, even though both peak pressures predicted by the present method and FD are almost the same, the total load compared with the previous case does not change significantly. The load directions however have a larger difference (5.5°). In brief, the film compressibility effects reduce the pressure peaks in the bearing and also produce a change in the pressure distribution phase. Another effect, this time related to the numerical scheme, resides in the fact that when the value of the bulk modulus increases, the diffusion velocity increases. This leads to a smaller maximum time step for the scheme to be stable. The method more readily "handles" compressible fluids. Note that, although the bulk modulus value for the oil used by Dimofte is not known, the first case ($\beta = 1.2105 \cdot 10^8$ Pa) probably is a more realistic value. Also, the code based on the present method uses a film thickness distribution calculated by Dimofte considering the elastic deformation of the bushing; this can also be a source of errors.

Misaligned Wave Journal Bearing

The misalignment of journal bearings can be defined using two parameters: the angle α between the centerline and the direction of the misalignment at the bearing center and the degree of mis-

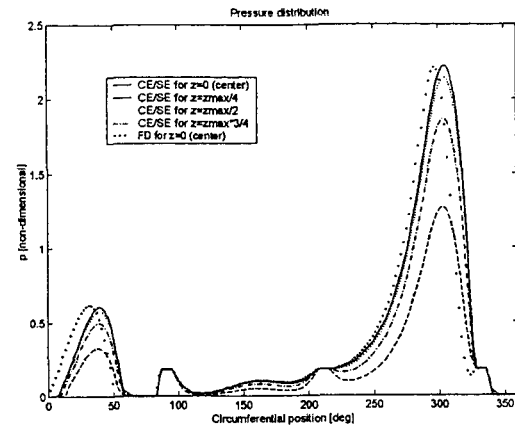


Fig. 6—Pressure distribution in a wave bearing.

alignment d_m that represents the proportion of the actual misalignment to the maximum possible. The maximum misalignment is restricted by the condition that at the bearing ends (in the axial direction) the film thickness reaches the value of zero. The physical conditions of the bearing are presented in Table 3. Because of the misalignment, the fluid film thickness is a function of both the circumferential and axial coordinates, so that for each value of the circumferential coordinate there is a domain of thickness variation, represented in dark color in Fig. 7(a). Both the aligned and misaligned bearing have the same film thickness distribution at the center plane (which is also the symmetry plane for the aligned case).

Three sections through the pressure distribution, at the mid-plane $z = 0$, and at mid-distance between this plane and the bearing ends, $z = \pm L/4$, are presented in Fig. 8(a). The maximum calculated pressure is 38.8 MPa (not seen in the figure). The same bearing with identical physical conditions but without misalignment has different values for the pressure distribution, as seen in Fig. 8(b) for the same sections (the pressure distribution is symmetric relative to the central plane $z = 0$). The maximum calculated pressure in this case is 23.2 MPa, at the symmetry plane. The cavitation and the full film regions for the misaligned and the aligned 3-wave bearing are presented respectively in Figs. 9(a), 9(b). The load is found to be 10,523 N for the aligned bearing and 22,115 N for the misaligned bearing, which shows that the misalignment may have a positive impact on bearing performance. This effect is due to the fact that, with misalignment, a region with smaller film thickness is present, compared with the same aligned bearing. This determines the development of higher pressures. At the same time, the region that has a larger film thickness develops cavitation, so that the pressure does not decrease the same amount as it increases in the smaller films thickness region.

CONCLUSIONS

The CE/SE method was applied for the first time to investigate two-dimensional flow in cavitated wave bearings. The theoretical formulation of the solution method was presented along with numerical results. The results were compared with the results obtained using other numerical algorithms. Using Elrod's formulation, discontinuities can appear at the reformation fronts, and the

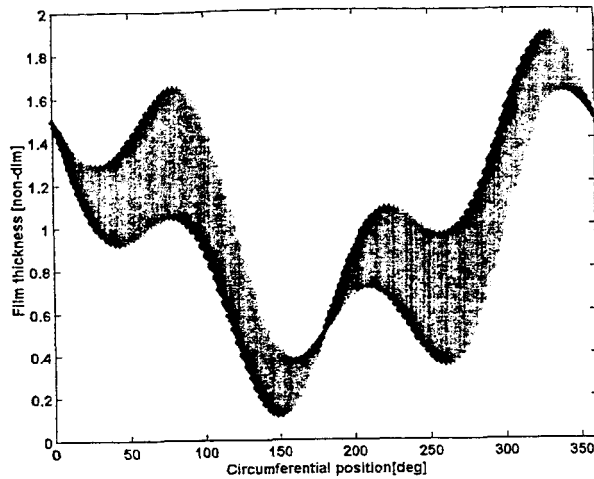


Fig. 7(a)—Fluid film thickness domain in a misaligned 3-wave bearing.

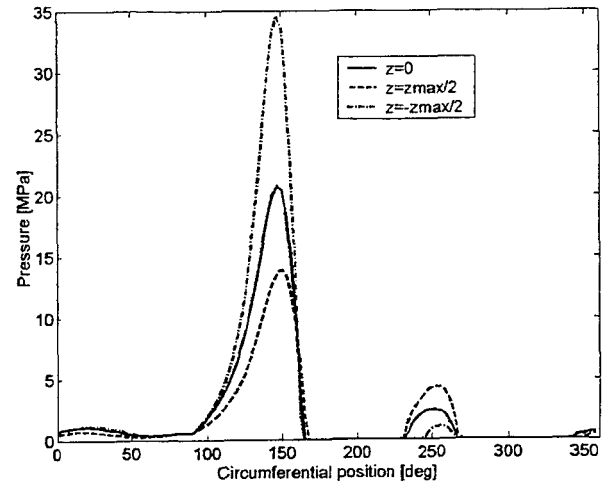


Fig. 8(a)—Pressure distribution in a misaligned 3-wave bearing at different axial sections.

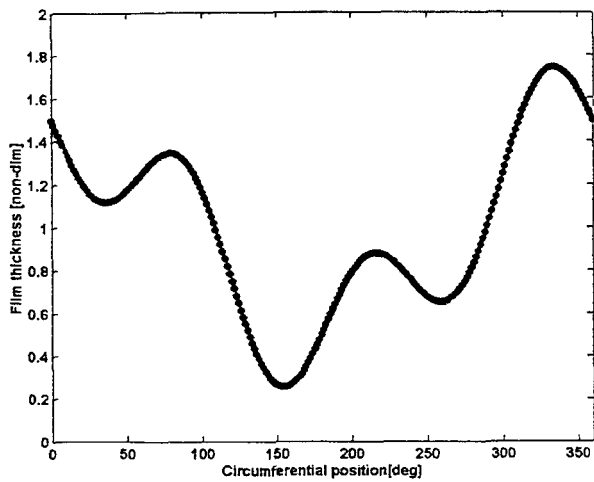


Fig. 7(b)—Fluid film thickness in an aligned 3-wave bearing.

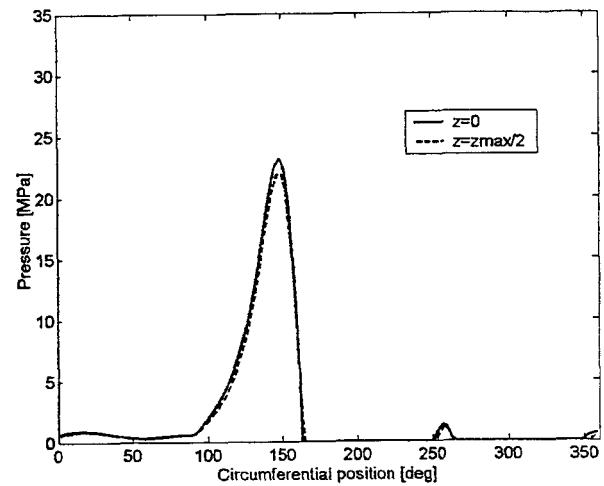


Fig. 8(b)—Pressure distribution in an aligned 3-wave bearing at different axial sections.

results presented show that the CE/SE method is able to capture these discontinuities without any special treatment, and thus it is potentially more accurate than "standard" methods. It is also important to recognize that the CE/SE method is conceptually simple and entirely explicit, which makes it also computationally efficient. However, the computational time is higher than for the steady solvers, which can give the results in seconds on modern personal computers, but it is comparable with other transient solvers (this statement is based on the comparison with the transient type difference code, which also uses the Elrod's formulation). The conclusion is that the method is a strong candidate to solve applications that require more precise results, such as accurate, robust computation of the cavitation boundaries, as well as to solve transient problems.

REFERENCES

- (1) Chang, S. C. and To, W. M. (1991), "A New Numerical Framework for Solving Conservation Laws – The Method of Space-Time Conservation Element and Solution Element," NASA TM 104495, NASA, Cleveland, OH.
- (2) Wang, X. Y., Chang, S. C. and Jorgenson, P. C. E. (2000), "Prediction of Sound Waves Propagating Through a Nozzle Without/With a Shock Wave Using the Space-Time CE/SE Method," NASA TM – 2000-209937.
- (3) Chang, S. C., Wang, X. Y. and Chow, C. Y. (1999), "The Space-Time Conservation Element and Solution Element Method: A New High-Resolution and Genuinely Multidimensional Paradigm for solving Conservation Laws," *Jour. of Comp. Phys.*, 156, 1, pp 89-136.
- (4) Chang, S. C., Loh, C. Y., Yu, S. T., Himansu, A., Wang, X. Y. and Jorgenson, P. C. E. (1997), "Robust and Simple Non-Reflecting Boundary Conditions for the Space-Time Conservation Element and Solution Element Method," AIAA Paper, 97-2077.
- (5) Jakobsson, B. and Floberg, L. (1957), "The Finite Journal Bearing Considering Vaporization," *Trans. of Chalmers University of Technology*, Gothenburg, Sweden, 190.
- (6) Olsson, K. O. (1965), "Cavitation in Dynamically Loaded Bearings," *Trans. of Chalmers University of Technology*, Gothenburg, Sweden, 308.
- (7) Elrod, H. G. (1981), "A Cavitation Algorithm," *ASME Jour. of Lubr. Tech.*, 103, 3, pp 350-354.
- (8) Vijayaraghavan, D. and Keith, T. G. Jr. (1989), "Development of a Cavitation Algorithm," *Trib. Trans.*, 32, 2, pp 225-233.
- (9) Vijayaraghavan, D., Keith, T. G. Jr. and Brewster, D. E. (1991), "Extension of Transonic Flow Computational Concepts in the Analysis of Cavitated Bearings," *ASME Jour. of Trib.*, 113, 3, pp 539-546.

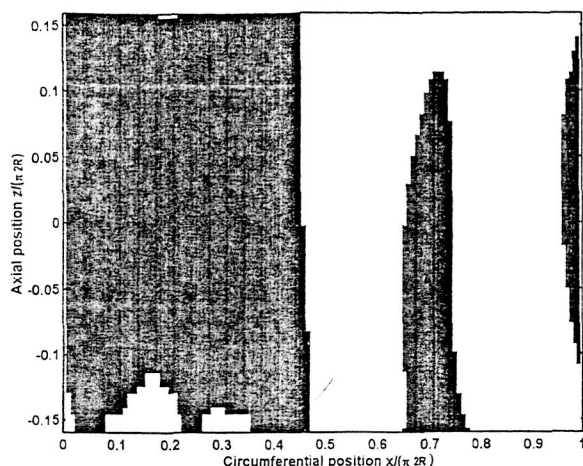


Fig. 9(a)—Cavitation map in a misaligned 3-wave bearing (full film region shown in dark color).

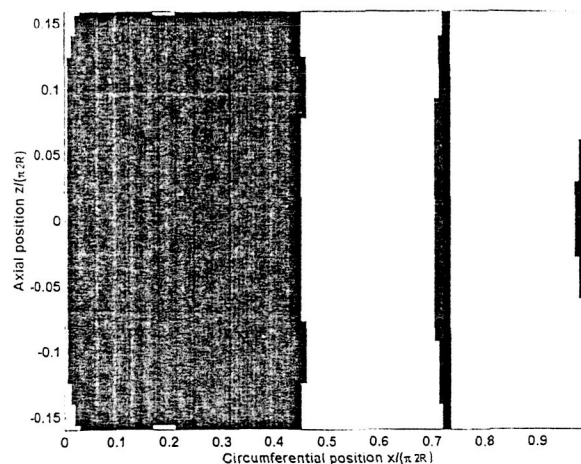


Fig. 9(b)—Cavitation map in an aligned 3-wave bearing (full film region shown in dark color).

- (10) Cioc, S. and Keith, T. G. (2002) "Application of the CE/SE Method to One-Dimensional Flow in Fluid Film Bearings," *Trib. Trans.*, 45, 2, pp 169-176.
- (11) Chang, S. C., et al. (1998), "Fundamentals of CE/SE Method," NASA TM-1998-208843, NASA, Cleveland, Ohio.
- (12) Liu, N. S. and Chen, K. H. (2001), "An Alternative Flow Solver for the NCC - the FLUX Code and its Algorithm," *AIAA Paper 2001-0973*.
- (13) Tannehill, J. C., Anderson, D. A. and Pletcher, R. H. (1999), *Computational Fluid Mechanics and Heat Transfer*, Second Edition, Taylor and Francis, pp 84-91, 177-274.
- (14) Vijayaraghavan, D. (1989), "New Concepts in Numerical Prediction of Cavitation in Bearings," Ph.D. Dissertation, The University of Toledo.
- (15) Dimofte, F., Proctor, M. P. and Keith, T. G. (2000), "Wave Fluid Film Bearing Tests for an Aviation Gearbox," NASA TM-2000-209766, NASA, Cleveland, Ohio.
- (16) Yang, D., Yu, S. and Zhao, J. (2001), "Convergence and Error Bound Analysis for the Space-Time CESE Method," *Numer. Methods Partial Differential Eq.*, 17, pp 64-78.